Benchmarking of Coatings for Cathode Active Materials in Solid-State Batteries Using Surface Analysis and Reference Electrodes

Jonas Hertle, Felix Walther, Teo Lombardo, Christine Kern, Boris Pavlovic, Boris Mogwitz, Xiaohan Wu, Holger Schneider, Marcus Rohnke, and Jürgen Janek*

ABSTRACT: Fast and reliable evaluation of degradation and performance of cathode active materials (CAMs) for solid-state batteries (SSBs) is crucial to help better understand these systems and enable the synthesis of well-performing CAMs. However, there is a lack of well-thought-out procedures to reliably evaluate CAMs in SSBs. Current approaches often rely on X-ray photoelectron spectroscopy (XPS) for the evaluation of degradation. Unfortunately, XPS sensitivity is not very high, and minor but relevant degradation products may not be detected and distinguished. Furthermore, degradation caused by the current collector (CC) itself is usually not distinguished from CAM-induced degradation. This study uses a modified CC, which allows us to separate electrochemical degradation caused by the CC from degradation at the CAM itself. Using this CC, we present an approach using time-of-flight secondary ions mass spectrometry (ToF-SIMS) that offers high sensitivity and reliability. Principal component analysis (PCA) is applied to differentiate secondary ions as well as identify those mass fragments that correlate with degradation products. This approach also enables distinguishing between different pathways of degradation. To evaluate the kinetic performance of the samples, three-electrode rate tests are performed. Electrochemical characterization evaluates the kinetic performance of the samples under investigation. The samples are finally rated with a score that allows a reliable comparison between the different materials and offers a complete picture of the materials′ characteristics in terms of electrochemical performance and degradation.

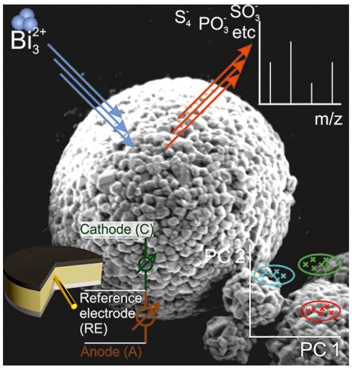

KEYWORDS: *solid-state battery, sulfide electrolyte, solid electrolyte, three-electrode setup, degradation, coating*

INTRODUCTION

Solid-state batteries (SSBs) are potentially able to surpass liquid-based lithium-ion batteries with increased energy and power density.[1−3] In SSBs, the liquid electrolyte is at least partially replaced by a single ion conducting solid electrolyte (SE).[4−6] In SSB cells, a dense solid electrolyte (SE) separator separates the anode and the cathode and thus stops any chemical crossover. In academic research, various negative electrode materials are used. The two-phase systems In/InLi and $Li_4Ti_5O_{12}/Li_7Ti_5O_{12}$ (LTO) are often chosen because of their constant electrode potentials independent from the state-of-charge (SOC) and their excellent stability together with SEs.[7−10] Lithium metal provides the highest specific capacity and leads to a high energy density of full cells.[11] Recently, silicon gained attention for use as an anode material in both LIBs and lithium SSBs.[12] A high specific capacity of 3590 mAh/g and its low potential of 0.4 V versus Li^+/Li make it suitable for high-energy density applications without the risk of dendrite formation.[13] Although first investigations of the Li−Si system date back as far as 1976 and first applications were presented more than 20 years ago, the use of the materials remains challenging.[14−16] High volume changes of up to 300% makes silicon electrodes with a long cycle life challenging, and a trade-off between a high volumetric energy density and long cycle-life has to be found.[12]

As cathode active materials (CAM), mostly layered oxides ($Li_xNi_yCo_zMn_{1\text{-}y\text{-}z}O_2$, NCM) and $LiFePO_4/FePO_4$ are used.[17−21] These materials provide the best energy densities for SSB and offer high potentials as well. For SEs, usually three groups are distinguished: first, oxides, such as cubic $Li_{6.25}Al_{0.25}La_3Zr_2O_{12}$ (LLZO) and $Li_{1+x}Al_xTi_{2-x}(PO_4)_3$ (LATP).[22−26] Despite their good electrochemical stability, their use is hampered by an ionic conductivity (usually <1 mS/cm) that is too low for high-energy and high-power composite electrodes, and their difficult processability due to their hardness and brittleness. Polymer electrolytes like poly(ethylene oxide) (PEO), for example, with lithium bis(trifluoromethane)sulfonimide (LiTFSI) as conducting salt, have excellent mechanic properties and processability.[27−31] However, the ionic conductivity is even lower at room temperature and the transference number of the Li^+ ions is small ($\sigma < 1$ mS/cm at 80 °C, $t_+ \approx 0.2$).[32] Thiophosphates (often also named as sulfides for simplicity) and ordered solid solutions with halides or metal sulfides such as Li_6PS_5Cl (LPSCl)[33] or $Li_{10}GeP_2S_{12}$ (LGPS)[34] are often seen as the most promising candidates because of their superior ionic conductivity of up to 32 mS/cm at room temperature and their good mechanical properties.[35]

The combination of thiophosphate-based solid electrolytes and NCM active materials, however, leads to different types of degradation.[36,37] First, morphological degradation takes place. This is due to the expansion and contraction of the CAM during charge and discharge, which leads to contact loss and cracking of the active materials' particles ultimately leading to high overpotentials and a lower practical capacity in the cell.[8,18] Second, when used in cathode composite electrodes, thiophosphate SE tend to decompose at high potentials, forming reactive oxygen and posing problems with long-term stability. Coatings of CAMs are a widespread approach to mitigate the degradation at the interface between the CAM and SE.[38,39] Additionally, they are used to increase the rate capability of the system by lowering the charge-transfer resistance between the CAM and the SE. Examples for coatings of cathode active materials are found frequently in the literature and the need for coatings of CAMs in all solid-state cells was already recognized by Ohta et al. in 2007.[38] The analyses reported in literature usually focus on the evaluation of a single coating in comparison to a not intentionally coated material, namely, a CAM with natural surface residues such as Li_2CO_3 and LiOH. These analyses are often combined with electrochemical tests such as electrochemical impedance spectroscopy (EIS), rate tests, and long-term cycling as well as post-mortem analysis with X-ray photoelectron spectroscopy (XPS) and time-of-flight secondary ion mass spectroscopy (ToF-SIMS).[10,37,38,40−44]

Since cathode degradation is caused both by morphological degradation of the CAM as well as by chemical degradation and as these contributions are not further differentiated, it is often unclear which factors contribute to a well working coating. Furthermore, coating compositions are difficult to assess due to the nature of only several nanometer thin films.[45] The positive effects of a coating are mostly attributed to their bulk properties, although the exact composition is unclear as lithium residual compounds can become part of the actual coating. Effects like the microstructure, residues on the CAM surface, and exact stochiometric compositions are not taken into consideration. Due to these limitations, only general and unspecific statements about coatings are found in the literature. It remains unclear which coating parameters, such as the coating thickness, ratio of precursor materials, annealing temperature, and so on, are leading to the best results. Finding optimal coatings is therefore quite difficult, and fundamental knowledge on the mechanism of the function of coatings is still mostly unknown. Apparently, the previous analytical approaches are not sufficient to completely characterize a coating; better and more reliable techniques are needed to allow for a better understanding of the functionality of different coating materials and techniques.

In this paper, we describe a fast and reliable approach to investigate the degradation of thiophosphate solid electrolytes with ToF-SIMS, allowing a direct comparison of different coatings. A full characterization includes the analysis of the coating microstructure as well as composition, electrochemical characterization such as the initial capacity, Coulombic efficiency, and rate tests as well as analysis of the degradation products caused by electrochemical and chemical decomposition at the SE|CAM interface. Structural degradation such as cracking and contact loss between the SE and the CAM is not included here as this highly depends on the CAM, the SE, and other additives used in the cell as well as the pressure that is applied during cycling. This is also why this study does not include long-term cycling data. According to the literature, the morphological degradation in SSBs can be severe. This effect is dominated by the choice of SE, specifically the crystallinity of SE, and the choice of additives. The addition of flexible binders, for example, reduces the effect of morphological degradation.[18] Introducing a binder to the cathode composite complicates the cathode composite further and makes the analysis more complicated. Here, we reduce the complexity of the system as much as possible without compromising the functionality of the cell; our target is the role of the coating.

Our strategy to investigate degradation in all-solid-state cells relies on a straightforward workflow: Electrochemical degradation is quantified by a novel ToF-SIMS analysis approach with higher sensitivity and less variance in the data by using a modified CC. Electrochemical measurements and rate tests are performed using a three-electrode setup to secure that only the cathode kinetics is investigated. No further additives are used to make sure that the differences in the performance arise from the differences in the active material itself. Combining both ToF-SIMS and electrochemical data allows for a complete assessment of the active material. Results are displayed in a radar chart that represents the effect of the coating on the interfacial degradation and the performance. This allows a fast comparison of different coatings and paves the way to finding the best coating for high-performance NCM composite cathodes.

EXPERIMENTAL SECTION

Materials. For the fabrication of all-solid-state battery cells, commercially available crystalline SE Li_6PS_5Cl with a measured ionic conductivity of $\sigma = 1.4$ mS/cm (NEI Corp., NJ, USA) was used without further modification. The Li_6PS_5Cl SE was received and stored in an argon-filled glovebox to maintain its integrity with impurity levels of oxygen ($p(O_2)/p < 1.0$ ppm) and water vapor ($p(H_2O)/p < 1.0$ ppm) being meticulously controlled. Prior to assembly, the indium foil (100 μm thickness, chemPUR, Germany) was subjected to vacuum-drying at 60 °C for at least 48 h. The lithium metal (abcr GmbH, Germany) used in this study was also stored in the argon-filled glovebox. The lithium foil was prepared by compressing small pieces (~5 mg) of lithium between pouch bag foils, resulting in a final thickness of approximately 200 μm. Out of these foils, discs with a 4 mm diameter were punched out. The CAMs were provided by BASF SE and underwent vacuum-drying at 250 °C for 12 h prior to utilization. The uncoated CAM is $LiNi_{0.85}Co_{0.10}Mn_{0.05}O_2$ (NCM85, d_{50} = 3.5 μm, d_{90} = 5.0 μm), and all other coated CAMs were made using this base CAM.

Cell Setup. The basic cell setup used in this study can be found in previous publications.[7,46] A few modifications were applied to the setup to better suit the needs for this study which are described below.[47]

Current Collectors (CCs). CCs for three-electrode measurements were made of stainless steel with a polished surface toward the SSB pellet to ensure maximum surface smoothness and homogeneity of the pellets built. All CCs were polished with a 250 nm polycrystalline diamond suspension in the last step, and only freshly polished CCs were used for cell construction.

CCs for ToF-SIMS measurements were produced by gluing an Al_2O_3 cylinder into a stainless-steel CC as shown in Figure 1. These

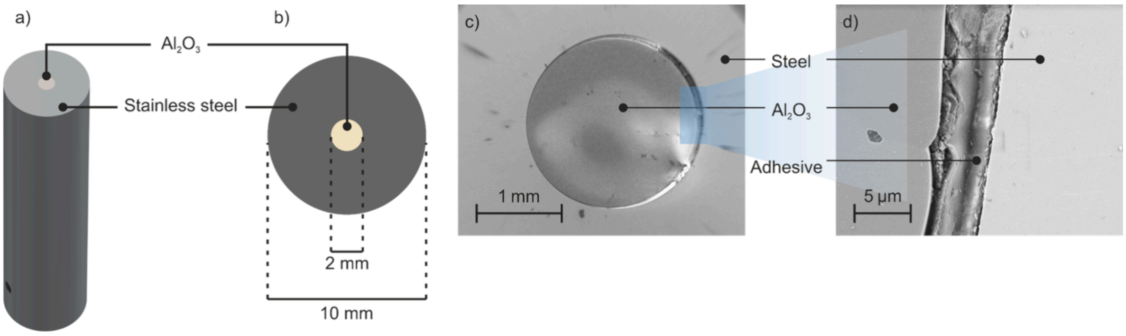

Figure 1. Modified CC were used for ToF-SIMS analysis. The inner part of the CC consists of Al_2O_3, which is neither ionically nor electronically conductive. (a, b) Different schematic views on the steel CC rod; (c) top view and (d) cross section of the CC with the alumina area (optical micrographs).

CCs were subsequently polished with the same procedure as that for the pure steel CCs.

Two-Electrode Setup and Cycling. Cells for degradation studies with ToF-SIMS were built according to the following procedure. 60 mg of Li_6PS_5Cl was pressed with a hand-press to form a SE separator layer. On top of the resulting pellet, 12 mg of the cathode composite (80 wt:20 wt CAM:SE) was distributed homogeneously, and the whole pellet was pressed at 374 MPa for 3 min. Afterward, indium foil (9 mm diameter, 100 μm thickness) and lithium foil (4 mm diameter, ~200 μm thickness) were placed on the other side of the solid electrolyte separator. The complete cell was held at a constant pressure of 50 MPa during cycling.

The cells were cycled at 0.05 C (1 C = 1.92 mA $\triangleq$ 2.44 mA/cm^2) for 1.5 cycles (charge−discharge−charge) and relaxed overnight until the start of the ToF-SIMS measurement.

Three-Electrode Setup and Rate Test. Three-electrode cells as described in the literature were used.[47] 60 mg of SE was hand-pressed, and the gold-wire reference electrode was placed on top. Another layer of 60 mg of SE was put on top, and the pellet was hand-pressed again. 12 mg of the cathode composite (67 wt:30 wt:3 wt CAM:SE:carbon) were distributed homogeneously on top, and the pellet was pressed at 374 MPa for 3 min. Afterward, indium foil (9 mm diameter, 100 μm thickness) and lithium foil (4 mm diameter, ~100 μm thickness) were placed on the other side of the solid electrolyte separator. The complete cell was held at a constant pressure of 50 MPa during cycling.

All cells were cycled at 0.1, 0.3, 1.0, and 2.0 C for two cycles each with a 2 h rest step in between each charge and discharge step.

ToF-SIMS Measurements. ToF-SIMS measurements were performed on a TOF-SIMS 5−100 by IonTOF GmbH Germany, which is equipped with a 25 keV Bi cluster primary ion gun for SIMS analysis and a dual-source column for depth-profiling with up to 2 keV by using O_2^+ or Cs^+.

The pellet that was used for ToF-SIMS mapping was prepared with a FIB in a Xe plasma FIB-SEM prior to the measurement as described below. The surface of the sample was flooded with low-energy electrons for charge compensation. The measurement was performed in the negative ion mode with 25 keV Bi_3^{2+} primary ions with a total ion dose of 5×10^{12} ions/cm^2, a cycle time of 60 μs in the spectrometry mode, and a mass resolution of ~6000. The data were analyzed with SurfaceLab 7.3 (IONTOF GmbH, Germany).

Comparing ToF-SIMS results requires scaling to account for the intrinsic heterogeneities of battery samples, including the presence of more or fewer particles/pores in certain regions or their different rugosity/topography, which can shield part of the ions generated through the first ion beam, leading to fewer secondary ions (SI) detected by the analyzer.

Several procedures can be used for this purpose, the easiest being scaling the SI count by the total number of SIs detected during the measurement. Another (conceptually similar) approach consists of scaling by the number of SIs (peak area) associated with a given species. In the context of battery electrodes, a possible choice for this is a peak specifically associated with the active material. In both cases, however, the data are scaled using the SIs collected over the entire region of analysis, therefore falling short in accounting for the heterogeneities inside the region of analysis (i.e., CAM-related SI signal being much higher in the subregion where a CAM particle stands and lower in subregions containing pores).

Analyzing smaller regions would overcome or at least minimize this limitation but at the expense of representativeness. Alternatively, it is possible to subdivide the region of analysis (in our case, 150 × 150 μm^2) into n pixels (in our case, 256 × 256) and analyze the single spectrum obtained by each of those rather than the overall spectrum. In other words, it is possible to scale each peak of each spectrum of each pixel by the total ion count (or by the ions associated with a reference species) measured from that same pixel. Afterward, the scaled value of each pixel is summed to reconstruct the data representative of the entire region of analysis. This approach can therefore combine the representativeness brought by the analysis of a relatively large area with the higher accuracy offered by consideration of its local heterogeneities.

Pixel-by-pixel normalization was used for the data analysis in this study. The analysis was performed through an in-house Python code, which performed the pixel-by-pixel analysis on all the peaks identified as relevant.[48] The data are scaled by either the total ion count or a reference species associated with the CAM (in our case, NiO_2^-), offering both of these results. In addition, for each sample, 14 different regions were analyzed to obtain statistically relevant information. The code automatically compares all the results obtained by the same sample and computes the associated statistics (minimum, maximum, average, median, standard deviation, first and third quartiles). Lastly, the code can compare the so-obtained results with a reference sample, allowing us to easily quantify the relative difference (%) between the reference and the other samples for each species analyzed. For better clarity, we provide only the average of the signals in the main part of this publication.

Orbitrap SIMS. The IONTOF M6 Hybrid SIMS has both a ToF and an OrbiTrap analyzer. In general, the high mass resolving performance ($m/\Delta m$ > 240,000 at m/z = 200) and high mass accuracy (<2 ppm) of the OrbiTrap analyzer enable accurate mass calibration and signal assignment and are therefore ideally suited to create a mass list for the investigation of degradation products in battery electrodes. Parameters for OrbiTrap mass spectra using a liquid metal ion gun (LMIG) as a primary ion gun were the following: 30 keV Bi_3^+ as the primary ion species with a primary ion current of 0.210 pA. The field of view was 150 × 150 μm^2 with a dose density of 1.00×10^{12} ions/cm^2. The ROI was rastered in the random mode with 51 × 51 pixels and a cycle time of 100 μs in the negative ion mode. For each sample, three measurements were acquired. The mass range was from m/z = 50 to 750 and the mass resolution (fwhm) was $m/\Delta m$ > 400,000 (at m/z = 78.95, PO_3^- signal). Using the OrbiTrap mass spectra, a mass list was generated, which was then applied to ToF-SIMS measurements. Deviations of the assigned masses were less than ±10 ppm. OrbiTrap mass calibration was performed once at the beginning of the measurement session using Ag clusters between Ag_1 and Ag_{15} from a reference sample. As the mass calibration remains stable for >25 h, no recalibration using known peaks from the spectrum was necessary. Data analysis of M6 Hybrid SIMS measurements was done with Surface Lab Software version 7.3 (IONTOF GmbH, Münster, Germany).

Principal Component Analysis. For principal component analysis (PCA), first, the intensities of each fragment as obtained from ToF-SIMS analysis (normalized to the total ion intensity) were exported for the cycled and uncycled samples. Both the cycled and uncycled samples were measured at $n \geq 10$ regions for better reproducibility. As the intensities of different fragments may vary by multiple orders of magnitude, the PCA was performed in relative rather than absolute terms. In other words, for each fragment, the spectrum for which the highest intensity was found was used as a relative reference. The value of the area underneath this peak was then scaled to 1, and all of the intensities of the same peak for the other spectra were scaled accordingly. This approach ensures that the PCA is not dominated by the SI with the highest intensity and allows focusing on the relative differences between cycled and uncycled samples.

The PCA loadings (representing the importance of each SI in describing the differences between the analyzed samples) were then used to evaluate the effectiveness of coatings to prevent (electro)-chemical degradation. This procedure was carried out with a python code that is available on GitHub.[49] A complete mass list used in this study can be found in Table S1.

Calculation of Degradation Scores. To estimate the degree of degradation that occurred in the various samples, a raw degradation score DS_{raw} is introduced as outlined in eq 1, where n is the number of measurements for a particular sample, m is the specific measurement spot, f is a fragment, l is the loading of that fragment, and v is the normalized intensity of that fragment obtained from ToF-SIMS analysis.

$$\mathrm{DS}_{\mathrm{raw}} = \frac{1}{n} \sum_{\mathrm{m}} \sum_{f} l \times v \tag{1}$$

Afterward, the raw scores DS_{raw} were scaled such that the uncycled sample has a value of 0 and the uncoated cycled samples have a value of 1, resulting in the degradation score DS. Several degradation scores were computed with a general degradation score where all the fragments are considered for the score as well as specific degradation scores where only certain fragments are taken into consideration. For the polysulfides, phosphate and sulfate degradation scores, namely, only the fragments labeled polysulfide PO_y and SO_y in Table S2, respectively, are taken into consideration.

XPS Measurements. X-ray photoelectron spectroscopy (XPS) measurements were conducted using a PHI5000 Versa Probe II system (Physical Electronics GmbH) instrument. All specimens were transferred from the glovebox to the spectrometer by utilizing a transfer system, ensuring continuous exposure to an argon environment throughout the process. The analysis employed monochromatic Al K_α radiation with an energy of 1486.6 eV. The X-ray source was operated at a power of 50 W and a voltage of 15 kV. The analysis beam had a diameter of 200 μm. To achieve charge neutralization, a dual beam system combining an ion beam and a low-energy electron beam was utilized. Pass energies of 23.50 were used. Data analysis was carried out using CasaXPS software (version 2.3.22, Casa Software Ltd.).

Prior to analysis, calibration of the XP spectra was conducted using a β-Li_3PS_4 reference material. The calibration was performed with respect to the signal of adventitious carbon at 284.8 eV. Subsequently, the signal position of the primary component of the S 2p signal corresponding to the $(PS_4)_3^-$ units was determined. The XP spectra of the composite cathodes were calibrated based on the main component of the β-Li_3PS_4 reference, thereby mitigating potential surface effects.

Signal fitting was executed using a Shirley background and GL(30) line shapes. Standard fitting constraints were implemented, including theoretical signal area ratios dependent on the orbital (e.g., p orbitals 1:2) and constraints on the full width at half-maximum (fwhm), and referenced to published values for spin−orbit splitting.

SEM and FIB-SEM Measurements. The SSB pellet was fixed to the sample holder using nonconductive tape. To ensure minimal exposure to air, all samples were directly transferred using a LEICA EM VCT500 transfer system, ensuring a transfer process without contact with air or moisture.

Focused ion beam (FIB) craters were generated using an XEIA3 Triglav instrument from Tescan utilizing a 30 kV Xenon plasma FIB operating at a current of 1 μA. Subsequent polishing of the craters was performed at 30 kV and 100 nA. FIB-scanning electron microscopy (SEM) measurements were conducted using a XEIA3 Triglav system from Tescan. SEM images were acquired at a 3 kV beam energy with a current of 290 pA, employing both a secondary electron detector and a backscattered electron (BSE) detector.

Further SEM measurements were carried out using a Zeiss Merlin Gemini instrument. Electron images were obtained using either a secondary electron or BSE detector.

RESULTS AND DISCUSSION

Experimental Design. *Two Pathways of Degradation.* In ToF-SIMS, a so-called primary ion beam scans the sample surface. During a collision cascade between primary ions and the sample surface among neutrals and electrons, SIs are also formed and collected by an electric field. Finally, the SIs are analyzed by their mass/charge ratio and detected locally resolved. A detailed introduction of the application of SIMS in battery research can be found in a publication by Lombardo et al.[48] For ToF-SIMS measurements, a modified CC was used as shown in Figure 1. Previous results show that there are two main pathways of degradation in solid-state cathode composites of thiophosphate-type SEs. One is arising from the SE being in contact with the CC and the other one is arising from the SE being in contact with the CAM particles.

Degradation at the Current Collector. Degradation arising from contact with a CC mainly leads to the formation of polysulfides, that is, oxidation of sulfur. This can be seen in XPS measurements as a shoulder in the S 2p signal at higher binding energies at around E_B = 163−165 eV as shown in Figure 3. This degradation occurs independently from the CAM as the surface of the cathode composite is always in contact with the CC and changes only slightly when different CAMs are used. Small differences in this degradation signal can arise from deviations in the electronic conductivity of the CAM surface as the electronically conductive CAMs serve as CCs themselves.[50] This signal of oxidation products is often used nonetheless to quantify degradation in a cathode composite despite its presence in any case.

Degradation by Oxygen. The other pathway of degradation directly at the SE|CAM contact leads to oxidation of the SE by oxygen, and sulfite/sulfate (Li_xSO_y) and phosphite/phosphate (Li_xPO_y) compounds are formed. These compounds can theoretically be detected with XPS, but in practice, the signal-to-noise ratio of SO_x is usually too low. Therefore, only polysulfides and general PO_x species can be detected with XPS, which is mainly attributed to CC-driven degradation as pointed out above.

Limited Suitability of XPS Surface Spectra for Analysis. Because of the effects described above, the XP surface spectra of cathode composite pellets are not suited to investigate degradation in solid-state cells properly, and a distinction is possible only between samples with little degradation and severe degradation. The evaluation of finer distinctions, that is, differences between different coatings, is not possible, and distinctions between degradation pathways are not possible. This is shown in previous publications by Walther et al., where cathode composites were investigated with XPS and ToF-SIMS.[36,37,51]

Sputtering to Minimize Current Collector Effects. As stated above, the CC leads to degradation of the SE forming mainly oxidized sulfur species like polysulfides. Sputtering the surface of the cathode composite pellet that removes this degradation layer caused by the CC only resolves this issue partly. The surface of the cathode composite is rough despite using polished (roughness of <250 nm) CCs. This roughness is determined by the particle size of the CAM and SE used. In the present case, the CAM particle size was in the range of 1−5 μm.

Sputtering this surface removes only a part of the degradation layer caused by the CC as depicted in Figure 2. Additionally, sputtering always alters the chemical composition of the investigated surface, which complicates analysis even further. These issues can be avoided when a part of the sample is not contacted by the CC, that is, it is only contacted by a nonconductive and inert material. In this work, this is achieved by using a modified CC with an outer stainless steel section and an inner Al_2O_3 section. The inner Al_2O_3 part is both electronically and ionically insulating, chemically inert, and mechanically stable.

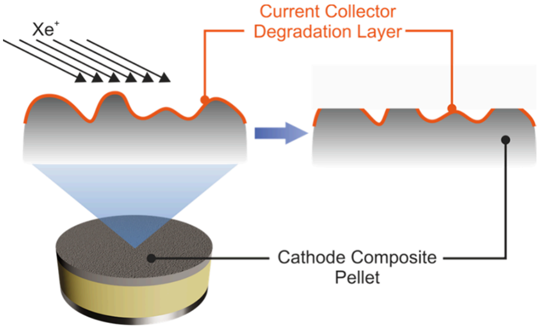

Figure 2. Sputtering the surface of a cathode composite pellet removes the degradation layer on top of the cathode composite pellet and leads to analytical results that are difficult to interpret due to uneven sputter removal.

Although this inner part is not directly contacted to the CC, the CAM particles are charged and discharged through contact with other active material particles due to their good electronic conductivity. As long as the CAM particles form a percolating network, the CAM particles in the inner section can be charged and discharged. Using a high loading of the active material (80:20 wt:wt, 63:37 vol:vol) ensures that all CAM particles are connected via their percolation network, and low currents during charging and discharging (0.05 C, 122 $\mu A/cm^2$) ensure negligible influence of overpotentials on the electrodes. This ensures that the SE on the surface of the pellet is subjected only to degradation caused by the CAM and not due to degradation caused by the CC. Separating CC-related degradation from CAM-related degradation allows for a better study of the CAM-related degradation.

Electrochemical Characterization besides SIMS Analysis. ToF-SIMS measurements offer information about the degree of degradation after cycling, and of course, the electrochemical performance of a coating is important as well. A very thick coating, potentially also a poorly conducting coating, for example, may lead to a low degree of degradation of the SE but would also perform electrochemically quite poor especially in high-current tests. A complete evaluation of any coating must therefore include electrochemical data as well, and in this study, we use rate tests for this evaluation. As we previously reported, it is important to use reference electrodes and three-electrode cells for the correct evaluation of the rate capability of an active material, thus avoiding any detrimental influence from the counter electrode (in the present case, the anode). The same setup as previously reported is used for this purpose.[47]

Long-Term Cycling. Previous publications in the field also report on long-term cycling as part of coating tests. There are several reasons why long-term cycling is not suited to the benchmarking presented in this study. In long-term cycling of SSBs, there is always an overlap between (electro)chemical and chemo-mechanical degradation. Due to the volume increase and decrease during cycling, the SE-CAM contact is partially lost in the electrode, leading to a decrease of the cell performance.[18] Investigating the long-term performance with the setup presented in this study (no binder, no conductive additives, crystalline SE), serious chemo-mechanical degradation is expected, and the difference introduced by the coating is small as the bulk active material is the same in every sample. The combined evaluation of degradation products and rate performance gives a sufficient and complete overview of the coating performance, and the comparison between different coatings becomes feasible. This approach also allows optimizing coatings, and balancing high-power performance and a long cycle life becomes possible.

In order to investigate and compare degradation of the SE in combination with different CAMs, different coatings were chosen. The coatings used for this comparison are listed in Table 1. These materials were selected as they represent commonly used coatings on the one hand ($LiNbO_3$ and ZrO_2) and, on the other hand, a promising new coating (X). This coating and the ZrO_2 coating were applied with two different thicknesses to investigate the influence of the coating thickness.

Table 1. CAMs Used in This Study[a]

CAM name	coating	amount
NCM uncoated	none	
NCM LiNbO3	$LiNbO_3$	1 wt %
NCM ZrO_2 thin	ZrO_2	1 wt %
NCM ZrO_2 thick	ZrO_2	5 wt %
NCM X thin	X	1 wt %
NCM X thick	X	5 wt %

[a] All coated samples are based on the uncoated material; that is, a coating was applied to the uncoated NCM.

Tof-SIMS and XPS. *Proof of Principle: XPS Analysis.* To show the difference in the inner and outer regions of the sample, XP spectra were recorded. The results are shown in Figure 3. The spectrum recorded on the outer steel contacted part shows oxidized sulfur at around E_B = 163−165 eV as a pronounced shoulder in the S 2p signal, indicating the formation of polysulfide species.[9] The phosphorus P 2p signal shows the oxidation of the phosphorus as well, which is visible as a shoulder in the range E_B = 132−136 eV. This becomes especially obvious when compared to the spectra recorded in the inner Al_2O_3 part, which shows a lower signal intensity in

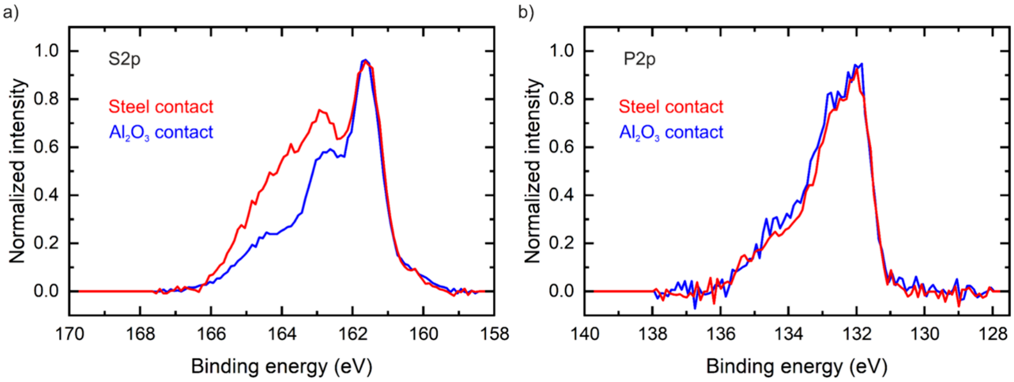

Figure 3. XP spectra (minimum to maximum normalized, background-subtracted) of a cathode composite contacted with the outer steel part (red) and Al_2O_3 inner part (blue). The S 2p signal (a) shows a pronounced shoulder at higher binding energies around 163−165 eV for the steel contacted spectrum. The P 2p (b) signal shows the same signal intensity for oxidized phosphorus species at higher binding energies of 132−136 eV as well. This is due to the contact with the stainless-steel CC, which leads to degradation of the solid electrolyte. However, the phosphorus degradation involves oxygen, which is the same for both the steel contacted and the Al_2O_3 contacted part of the sample. The graph without a background correction can be found in Figure S10.

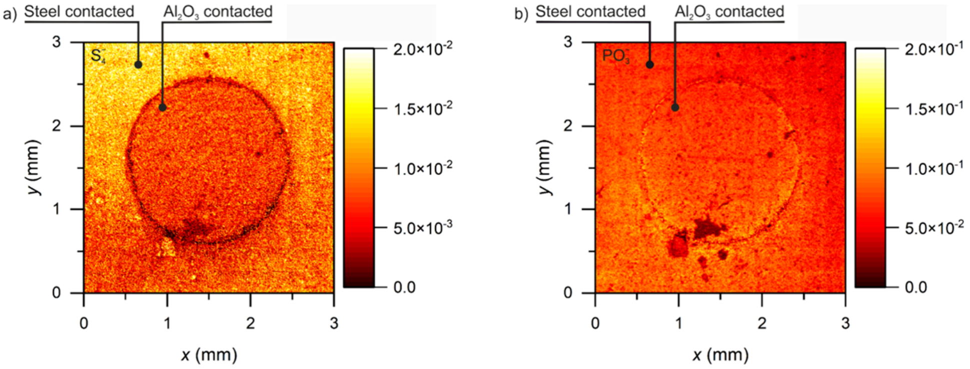

Figure 4. Large area SIMS scan of the cathode composite pellet, which was cycled with the modified CC. The image is normalized to the total ion intensity. (a) The S_4^- signal is much less pronounced in the inner part where the sample was contacted by Al_2O_3. As the S_4^- signal is indicative of polysulfide formation, which is driven by the CC, it can be concluded that this pathway of degradation is indeed suppressed in the inner part of the sample. (b) The PO_3^- signal is spread out equally throughout the whole pellet's surface. The PO_3^- signal is indicative of degradation driven by the oxygen containing CAM. As the CAM distribution is homogeneous throughout the whole pellet, the respective degradation products are spread out homogeneously as well. Furthermore, no significant change in the intensity can be observed, proving the concept of the modified CC.

this region and therefore lower amounts of degradation. The S 2p signal at around 169 eV is indicative of one of the known pathways of solid electrolyte degradation; however, this signal is hardly detectable in the recorded spectra.[9,36] Therefore, XPS is not suited to investigate coatings in solid-state cells as the compounds of the most interesting degradation pathway remain undetected, and the detected degradation products are mainly caused by the contact of the SE with the CC and are hence independent from the materials used.

Proof of Principle: ToF-SIMS. The working principle of the modified CC was further investigated by ToF-SIMS measurements. Large area scans of the inner Al_2O_3 and outer stainless-steel part were acquired. In these spectra, degradation products can be assigned to different fragments, that is, to SIs with different m/z ratios. Depending on the pathway of degradation, different degradation products form. CC-driven degradation leads to the formation of polysulfides, and these can be detected by S_x^- signals. As the inner part is contacted to Al_2O_3, the formation of polysulfides is suppressed in this area as can be seen in Figure 4a. The Al_2O_3 contacted part shows a smaller signal; however, the signal is not completely absent. This is due to two reasons. First, these fragments can be formed during a collision cascade with the Bi clusters even when no degradation products are present. The smaller the value x for the S_x^- fragment, the higher the probability that these fragments are formed during SIMS analysis; see Figure S3. For $x = 1$ and $x = 2$, no significant difference between the steel and the Al_2O_3 contacted area are observed (Figure S3a,b). For higher values ($x \geq 3$), the probability of these fragments being formed upon impact of the Bi clusters with the solid electrolyte becomes lower, and mostly degradation products are detected. For S_3^- and S_4^-, the difference between steel and the Al_2O_3 contacted area is easily detectable (Figure S3c,d). For even larger fragments such as S_7^- and S_8^-, the difference is still observable; however, the ionization probability gets lower and the signal-to-noise ratio of the mass spectrometric data is smaller. However, even for the signals where the difference between the inner and outer parts is observable, polysulfides are still detected in the inner Al_2O_3 region. This is because the CAM particles are electronically conductive and form a percolating network; that is, they act as CCs as described above. Because the CAM is in contact with the SE, polysulfides are formed as well. Due to the absence of the steel CC on top of the sample, the amount of polysulfides is reduced.

The distribution of oxygenated fragments such as SO_2^-, SO_3^-, PO_2^-, and PO_3^- can be evaluated in the same way. These

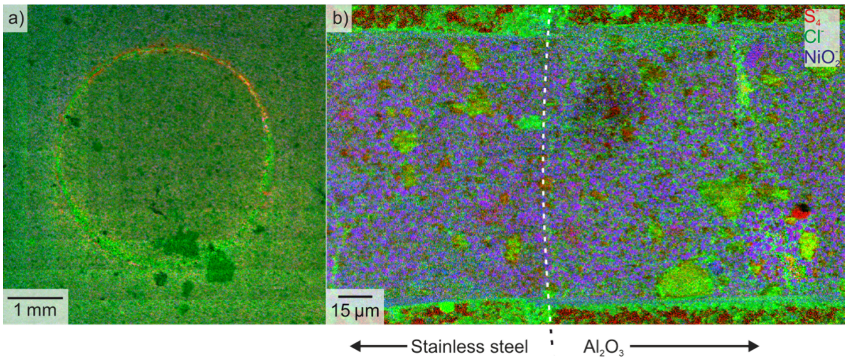

Figure 5. (a) Large-area scan of a cathode composite pellet without surface modifications. Here, mainly the SE shown in green (Cl^- signal) is visible. (b) High-lateral resolution ToF-SIMS image of a large area cross-section (FIB-cut with 5°) of a cathode composite pellet. The white dotted line marks the border between the steel and the Al_2O_3 contacts. CAM particles are distinctly visible in blue. The solid electrolyte is represented by the Cl^- signal shown in green. Single relatively large particles of SE are visible as well as the homogeneous distribution between the CAM particles in combination with degradation products shown in red.

degradation products are only formed in the presence of the active material as this is the only source of oxygen in the cathode. Therefore, if the CAM particles are connected through a percolation network within the electrode, the same amount of degradation products is expected on top of the electrode regardless of contact with Al_2O_3 or steel. In fact, there is no significant difference in the PO_3^- signal between the steel-contacted and the Al_2O_3-contacted regions in Figure 4b, confirming that there is no major difference in the amount of oxygenated degradation products. Figure S1 shows further signals SO_3^- and Li^- with no significant difference between the steel-contacted and the Al_2O_3-contacted regions. To further confirm the working principle of this analytical setup, the upper part of the pellet was removed with a low-angle FIB cut. The sample was tilted in a way that allowed a shallow cutting angle of only 10°. The cut was positioned at the edge between the steel and the Al_2O_3 contacted part of the pellet surface. This removes the upper few micrometers of the pellet and reveals a large cross-sectional area below. Potential differences caused by the different contact are now removed, and no more differences, both in polysulfide (detectable as S_4^-) and in oxygenated product formation (detectable as PO_3^-), are expected. This is indeed the case as can be seen in Figure 5 where an overlay of NiO_2^-, S_4^-, and Cl^- represents the CAM, the SE, and the degradation products, respectively. Figure S4 shows the same representation but with PO_3^- as a degradation product, and Figure S2 shows the SEM image of the FIB cut. In this case as well, no difference is observed between the inner and outer regions of the sample.

Mass Spectrometry with High Mass Resolution. While ToF-SIMS provides fast and reliable results for the benchmarking of degradation in solid-state battery cathodes, it is difficult to assign all signals precisely to specific fragments. For example, the difference in the masses of O_2^- and S_2^- is very small with $m/z = 31.989830$ and $m/z = 31.972072$, respectively. Therefore, signals such as SO_2^- and S_2^- that have almost similar m/z ratios are hard to distinguish in ToF measurements due to the low mass resolution of approximately 6000. Furthermore, ToF-SIMS suffers from decreased resolution due to the roughness of the sample surface. In order to clearly identify all signals in the measurement, it is necessary to measure the sample with higher mass resolution. To achieve this, one sample was measured with OrbiTrap-SIMS. The OrbiTrap detector allows a much higher mass resolution of up to 10^5, making it possible to identify all the signals observed in ToF-SIMS unequivocally. Additionally, the mass resolution of OrbiTrap-SIMS is not decreased by the sample surface roughness. The mass interval list obtained from the OrbiTrap measurement was then applied to all ToF-SIMS measurements, which strongly improved the quality of the analyses. This difference is also highlighted in Figure S6 in the Supporting Information.

ToF-SIMS Analysis Results. *PCA.* Previous ToF-SIMS studies on solid-state composite cathodes relied on picking relevant fragments manually for analysis. While this approach generally works sufficiently well, principal component analysis (PCA) can be used to identify all relevant fragments for degradation more reliably. For this purpose, an uncycled and a cycled sample were used for PCA with eight measurements for each sample. As in this case, only two different samples were investigated, the data can, as expected, be explained mostly by one principal component as shown in Figure 6.

The scores of principal component 1 show a clear distinction between the cycled and uncycled sample. Measurements of the cycled sample showed positive values for PC1 and negative values for the uncycled sample. PC2 and higher do not show any correlation of the SIMS data of the cycled and uncycled

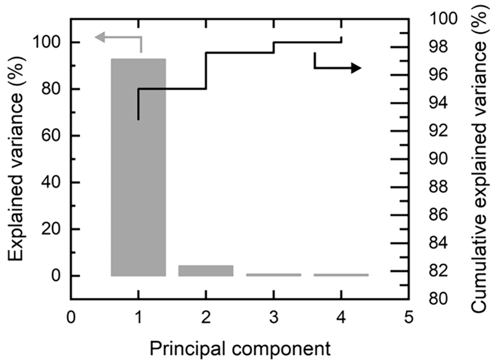

Figure 6. Variance and cumulative variance obtained by PCA performed on a cycled and uncycled cathode composite with uncoated CAM. As only two different samples were used, most of the variance in the data can be explained with one principal component. Most of the variance can be explained with only one principal component.

sample. Therefore, only PC1 and PC2 are shown here in Figure 7. Scores for PC3 and PC4 can be found in Figure S5.

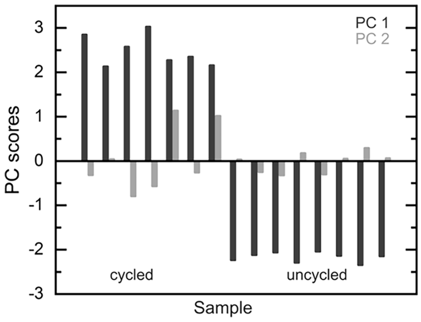

Figure 7. Scores for PC1 and PC2 for the cycled and uncycled sample. PC1 shows positive values for the cycled and negative values for the uncycled sample. The samples can be easily distinguished using PC1. PC2 shows no correlation between cycled and uncycled samples and can therefore not be used for distinction of the samples.

Because the scores for PC1 are clearly separated between the cycled and uncycled samples, the loadings of these PCs can be used to determine which fragments are indicative of degradation because the cycled samples are clearly more prone to degradation compared to the uncycled samples. Figure 8 shows the loadings for PC1 for the selected fragments.

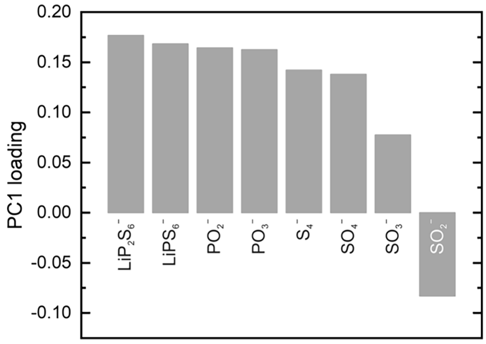

Figure 8. Loadings for PC1 are for selected fragments. The fragments with the highest loadings are shown as well as fragments that are commonly used to indicate degradation in cycled cathode composites.

The fragments with the highest loadings, namely, those fragments that are most indicative of degradation and other fragments that were used in previous studies, were chosen. A complete list can be found in Table S1. Some of the previously used fragments such as PO_2^-, PO_3^-, and S_4^- were found to be good indicators of degradation according to their PC1 loadings. However, further useful fragments could also be identified. SO_4^- can be used to identify oxygen related degradation, and $LiP_2S_6^-$ as well as $LiPS_6^-$ can be used to identify polysulfide formation. Moreover, other fragments such as SO_2^- can now be ruled out as indicators for degradation as the intensity of SO_2^- is actually inversely related to the presence of degradation products in the cathode composite.

PCA of Coated Samples. In addition to PCA of the uncycled and cycled sample, PCA was performed on all cycled samples as well. The goal here is to examine the coatings and try to find similarities and differences among the groups.

First, PCA was performed on the cycled (coated and uncoated) samples and the uncycled sample. The explained variance shown in Figure 9 indicates that at least over half of the data's variance is well explained with only one PC. At least three PCs are needed to describe the rest of the data sufficiently. The first PC separates the cycled sample from the uncycled sample, and the other PCs separate the cycled samples. Each sample forms a cluster, and PCA therefore allows grouping and separation of the cycled samples. The PC1 versus PC2 plots show this relation between the samples as shown in Figure 10. The higher PC versus PC can be found in Figures S7 and S8.

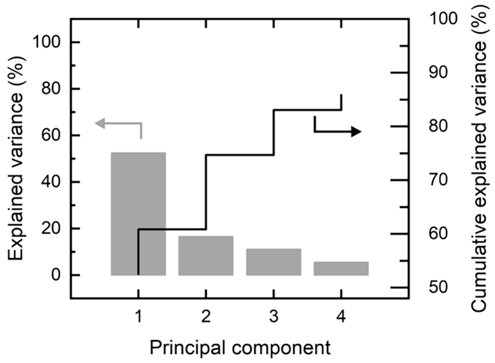

Figure 9. Explained variance of the PCA performed on cycled samples (coated and uncoated) and the uncoated sample. Multiple PCs are needed to explain the variance in the data.

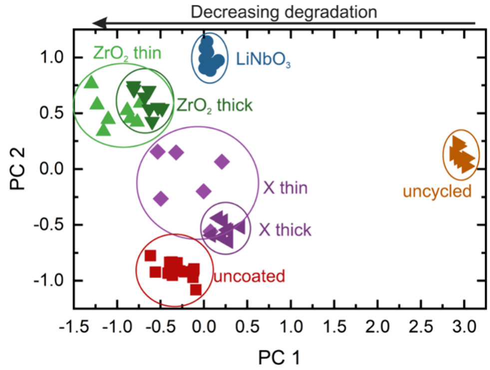

Figure 10. PCA of cycle-coated and uncoated samples. The strongest separation is present between the uncycled and cycled samples in PC1 as shown. The separations on PC2 are not as strong, but clustering of the different coatings is still observed on PC2. Plots for the other PCs can be found in Figures S7 and S8.

The loadings of this PCA shown in Figure S9 are very similar to the PCA performed with the uncycled and cycled (uncoated) samples only. To conclude, PC1 can be used as a general degradation marker. Here, a high score for PC1 is desirable as it indicates less degradation and a higher similarity to the uncycled sample. This allows scoring the performance of the coating in terms of degradation by simply evaluating the PC1 score. One can arbitrarily scale this score for better comparison, for example, here, the scores are scaled from 0 (for the uncycled sample) to 1 (for uncoated sample); therefore, low values in the degradation score are favorable over high values. The results of the overall degradation score are listed in Figure 11. These data show that not all coatings lead to less degradation and lower degradation scores. In this example, both CAMs coated with ZrO_2 actually lead to more

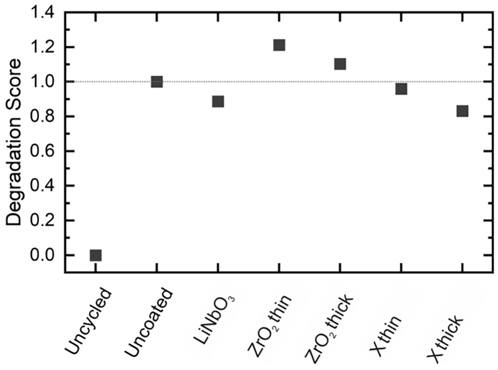

Figure 11. Degradation scores obtained from the PCA analysis of different samples. The values are scaled from 0 to 1, where 0 is assigned to the uncycled sample and 1 is assigned to the uncoated cycled sample. High values indicate high amounts of degradation and vice versa.

degradation compared to that of the uncoated sample. The best degradation score is obtained by the sample with the thick X coating and the $LiNbO_3$ coating. This degradation score, however, does not indicate which degradation pathway leads to higher or lower scores.

Detailed ToF-SIMS Analysis Results. While the PCA allows one to evaluate the samples in terms of degradation in general, further evaluation in terms of electrochemical and chemical degradation is not possible with PCA. For this purpose, the fragments require manual categorization. This categorization can be found in Table S2. With this categorization and the PCA results shown before, all fragments that are designated to a specific kind of degradation can be considered for evaluation instead of just taking a few representative fragments for quantification of degradation.

Here, two main pathways of degradation are considered. First, the electrochemical degradation leads to polysulfide formation. Fragments assigned to this pathway are labeled with "polysulfide" in Table S2. Second, chemical degradation leads to the formation of oxygenated sulfur and phosphorus compounds. Fragments assigned to these pathways are labeled with SO_y^- and PO_y^-. A detailed description of how the degradation scores are obtained is given in the Experimental Section.

The general degradation score shows stronger degradation for the $LiNbO_3$ and the ZrO_2 coatings, indicating higher amounts of degradation products for these samples. However, these values have to be interpreted with care. The PCA as applied here describes the data in terms of the highest variance when the intensity of each fragment is normalized to one. In other words, the fragments with the highest relative difference between the samples have the highest loading in PC1. PCA does not distinguish where this difference arises from. This is why further interpretation of the data is still necessary. In addition to the general degradation score, more specific degradation scores are introduced, namely, polysulfide degradation and sulfate and phosphate degradation scores. The fragments used for these degradation scores are chosen manually based on the chemical understanding of the cathode composite. Oxygenated sulfur compounds will lead to more fragments of the type $Li_{0/1}SO_x$, oxygenated phosphorus compounds will lead to fragments of the type $Li_{0/1}PO_x$, and polysulfide will lead to more fragments of the type $Li_{0/1}P_xS_y$.

Looking at the polysulfide formation in Figure 12b, it becomes clear why the ZrO_2 coatings have high general

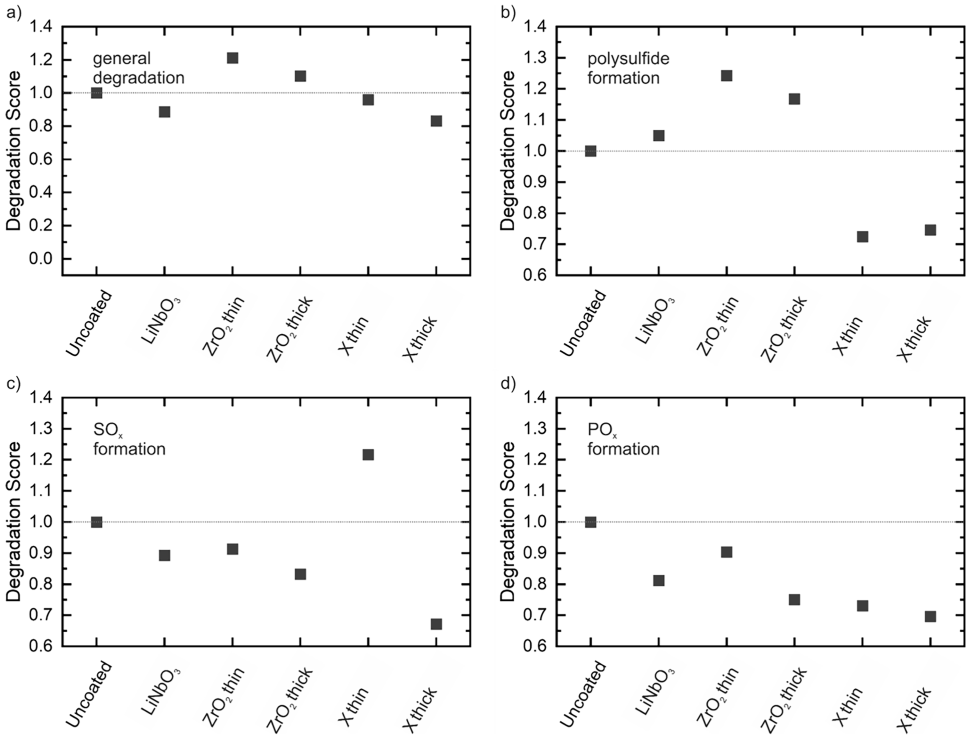

Figure 12. Specific degradation scores for specific degradation pathways. (a) Overall degradation score of the coatings. $LiNbO_3$ and ZrO_2 have higher degradation scores than the uncoated sample, indicating higher amounts of degradation. Only the X coatings show less overall degradation scores. (b) Polysulfide formation is suppressed in every coating except the thin X coating. (c, d) SO_x is suppressed in every coating except for the thin X coating, and PO_x formation is suppressed in every coating to different extents.

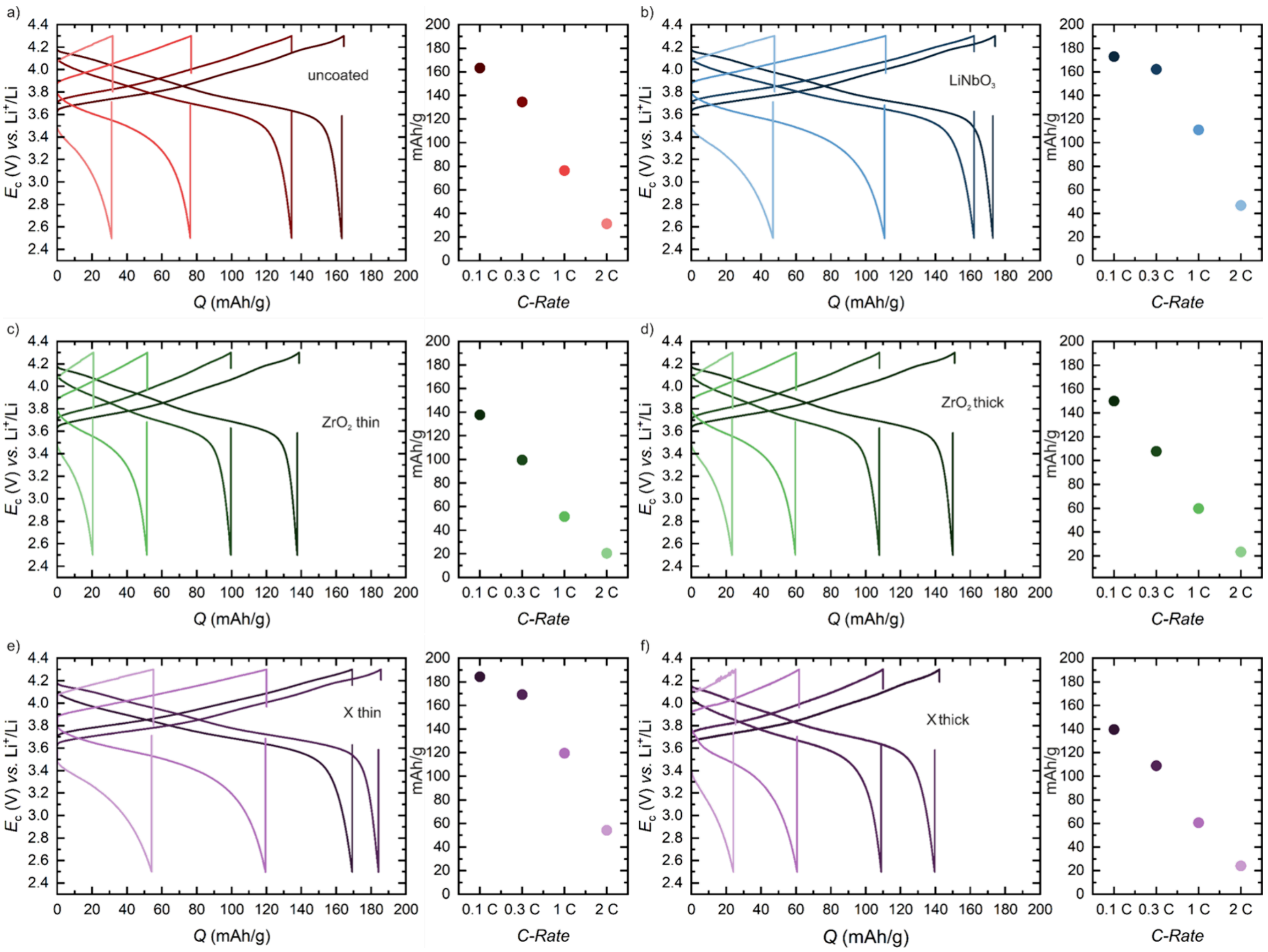

Figure 13. (a−f) Results of the rate tests performed on the different CAMs. The thin X (e) and LiNbO$_3$ coating (b) improve the electrochemical performance. The thick X coating (f) decreases the electrochemical performance despite showing good degradation results. The ZrO$_2$ (c, d) coatings decrease the electrochemical performance.

degradation scores. The polysulfide formation in these coatings is actually higher compared with the uncoated sample. The other coatings show slight (LiNbO$_3$) or substantial improvement (X) compared to the uncoated sample as shown in Figure 12. The increased or decreased polysulfide formation could be explained by the electronic partial conductivities (σ_{el}) of the respective coatings. According to Nakamura et al., a coating with a lower σ_{el} will protect the SE from electrochemical degradation while a coating with a higher σ_{el} will not protect the SE from electrochemical degradation.[52] The formation of oxygenated sulfur compounds is suppressed in every coating with the highest suppression being observed in the thick X sample. A similar trend is observed in the formation of oxygenated phosphorus compounds. The X coatings perform best, while all coatings reduce the amount of oxygenated phosphorus compounds.

Not surprising, in all degradation scores, the thick coatings show less degradation compared to their thin counterparts.

Rate Tests. Rate tests were performed for each active material in order to evaluate the electrochemical performance. The materials are compared with respect to their low-current (0.1 C) discharge capacity, their high-current (1.0 and 2.0 C) discharge capacity, and their capacity retention at high currents. Furthermore, the overpotential was measured (against a reference electrode). Uncoated NCM serves as a baseline measurement to which the other materials are then referenced.

Rate tests were performed to evaluate the kinetic performance of the coatings as well as the initial capacity they provide. The capacity retention at high currents (2.0 C) is used as a simple indicator for kinetic improvement or worsening of the CAM/SE system. Here, scores QS$_0$ and QS$_{ret}$ are introduced for the initial capacity and the capacity retention at 2.0 C, respectively, to allow for a quick overview over the electrochemical performance of the CAM. Again, the values of the uncoated NCM serve as reference data and their scores for the initial capacity and capacity retention are set to 1. The values for the other CAMs are calculated relative to the uncoated material, cf. eqs 2 and 3.

$$QS_0 = \frac{\frac{Q_{0.1C}}{Q_{2C}}}{\frac{Q_{0.1C,uncoated}}{Q_{2C,uncoated}}} \tag{2}$$

$$QS_{ret} = \frac{Q_{ret}}{Q_{ret,uncoated}} \tag{3}$$

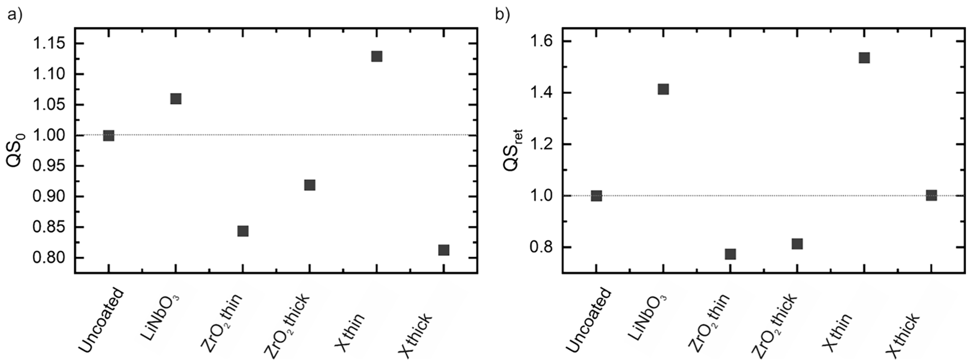

Figure 14. Scores for (a) initial capacity and (b) capacity retention at high currents. The ZrO_2-based coatings decrease electrochemical performance as well as the thick X coating. The other coatings, especially the thin X coating, led to an improvement in electrochemical performance.

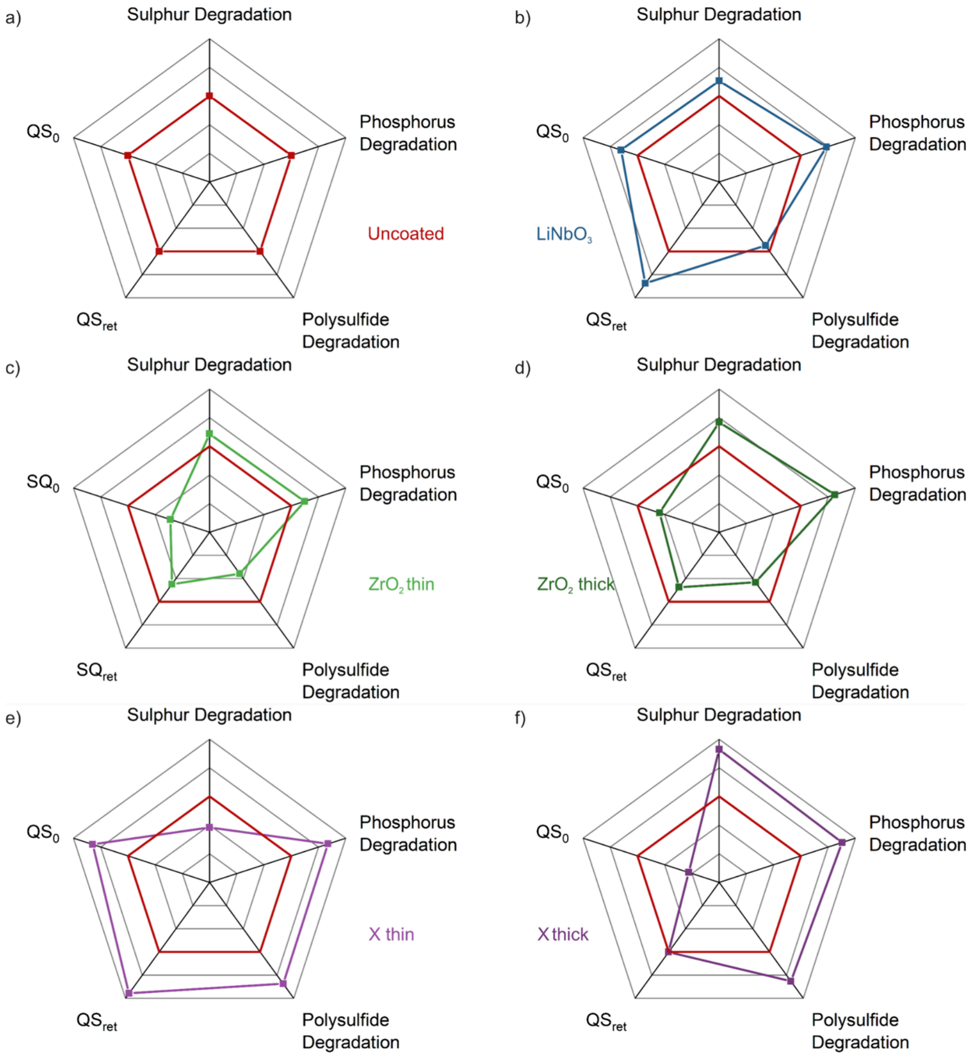

Figure 15. (a−f) Radar charts for the electrochemical and degradation performance of the CAMs used in this study. Only two coatings, namely, $LiNbO_3$ (b) and thin X (e), improve the electrochemical performance. The other coatings (c, d, f) do not lead to electrochemical performance improvements compared to the uncoated sample (a).

Out of the data given in Figure 13, the respective scores of QS_0 and QS_{ret} can be calculated. The results are shown in Figure 14. Only two coatings increase the initial capacity at 0.1 C, namely, $LiNbO_3$ and the thin X coating. The other coatings actually lead to a decrease in capacity. These results also highlight the importance of the thickness of the coating. For both the ZrO_2 and the X coating, the thick coating shows worse electrochemical performance probably due to the bad conductivity of the coating layer.

Radar Charts. The aforementioned results can be conveniently summarized in radar charts with each axis representing one score, resulting in a total of five axes/scores for each sample. The radar charts are presented such that values further from the middle represent favorable scores. Note that the scaling of these radar charts is arbitrarily chosen and that it can be adjusted to the specific needs of researchers working on similar benchmarking approaches.

Looking at the radar charts in Figure 15, it becomes immediately clear which coatings perform well and which coatings perform badly in different aspects.

SUMMARY AND CONCLUSIONS

In this study, a relatively fast and reliable way of benchmarking different coatings for CAMs in SSB is introduced based on the quantification of degradation products of the sulfide SE. First, the shortcomings of widespread techniques in the literature were discussed. In contrast to previous publications, the focus lies on getting reliable degradation and performance data instead of focusing only on certain aspects of the coating. Second, several coatings are compared, highlighting each of their advantages and disadvantages. Our study demonstrates how to utilize ToF-SIMS data effectively by using a PCA-based approach. This allows us to determine those fragments, namely, secondary ions, that are most relevant to quantify SE degradation as well as distinguish between different pathways of degradation. Using this approach, we found that some of the coatings do not mitigate degradation. Furthermore, we are able to determine which degradation pathway is actually responsible for the declining performance.

Second, precise electrochemical testing using three-electrode cells was performed. This allows for an accurate judgment of the kinetic capabilities of the different coatings. In fact, we found that not all coatings improve the performance. The X coatings reduced the degree of degradation for both the thick and thin coating layers. However, only the thin coating also improved the electrochemical performance. This highlights the need for systematic optimization of coating chemistries.

The approach presented here is widely applicable and can easily be adapted to other active materials and coating compositions. It relies on the high sensitivity and good spatial resolution of ToF-SIMS and thus cannot be achieved with other analytical techniques.

AUTHOR INFORMATION

Corresponding Author

Jürgen Janek – *Institute of Physical Chemistry, Justus Liebig University Giessen, D-35392 Giessen, Germany; Center for Materials Research (ZfM), Justus Liebig University Giessen, D-35392 Giessen, Germany; Battery and Electrochemistry Laboratory, Institute of Nanotechnology, Karlsruhe Institute of Technology (KIT), D-76344 Eggenstein-Leopoldshafen, Germany;* orcid.org/0000-0002-9221-4756; Email: juergen.janek@phys.chemie.uni-giessen.de

Authors

Jonas Hertle – *Institute of Physical Chemistry, Justus Liebig University Giessen, D-35392 Giessen, Germany; Center for Materials Research (ZfM), Justus Liebig University Giessen, D-35392 Giessen, Germany*

Felix Walther – *Institute of Physical Chemistry, Justus Liebig University Giessen, D-35392 Giessen, Germany; Center for Materials Research (ZfM), Justus Liebig University Giessen, D-35392 Giessen, Germany;* orcid.org/0000-0002-5843-4237

Teo Lombardo – *Institute of Physical Chemistry, Justus Liebig University Giessen, D-35392 Giessen, Germany; Center for Materials Research (ZfM), Justus Liebig University Giessen, D-35392 Giessen, Germany*

Christine Kern – *Institute of Physical Chemistry, Justus Liebig University Giessen, D-35392 Giessen, Germany; Center for Materials Research (ZfM), Justus Liebig University Giessen, D-35392 Giessen, Germany*

Boris Pavlovic – *Institute of Physical Chemistry, Justus Liebig University Giessen, D-35392 Giessen, Germany*

Boris Mogwitz – *Institute of Physical Chemistry, Justus Liebig University Giessen, D-35392 Giessen, Germany; Center for Materials Research (ZfM), Justus Liebig University Giessen, D-35392 Giessen, Germany*

Xiaohan Wu – *BASF SE, 67056 Ludwigshafen, Germany*

Holger Schneider – *BASF SE, 67056 Ludwigshafen, Germany;* orcid.org/0000-0002-8798-2961

Marcus Rohnke – *Institute of Physical Chemistry, Justus Liebig University Giessen, D-35392 Giessen, Germany; Center for Materials Research (ZfM), Justus Liebig University Giessen, D-35392 Giessen, Germany;* orcid.org/0000-0002-8867-950X

Notes

The authors declare no competing financial interest.

ACKNOWLEDGMENTS

Financial support by BASF SE within the International Network for Batteries and Electrochemistry and by Bundesministerium für Bildung und Forschung (BMBF) within the projects PROGRAL (no. 03XP0427) and the Cluster of Competence for Solid State Batteries (no. 03XP0433D) is acknowledged. Many thanks to the DFG for funding the Hybrid-SIMS under Grant No. INST 162/544-1 FUGG.

REFERENCES

(1) Janek, J.; Zeier, W. G. A Solid Future for Battery Development. *Nat. Energy* **2016**, *1* (9), 16141.

(2) Kim, K. J.; Balaish, M.; Wadaguchi, M.; Kong, L.; Rupp, J. L. M. Solid-State Li–Metal Batteries: Challenges and Horizons of Oxide and Sulfide Solid Electrolytes and Their Interfaces. *Adv. Energy Mater.* **2021**, *11* (1), 1–63.

(3) Kim, M.-J.; Park, J.-W.; Kim, B. G.; Lee, Y.-J.; Ha, Y.-C.; Lee, S.-M.; Baeg, K.-J. Facile Fabrication of Solution-Processed Solid-Electrolytes for High-Energy-Density All-Solid-State-Batteries by Enhanced Interfacial Contact. *Sci. Rep.* **2020**, *10* (1), 11923.

(4) Yu, X.; Bates, J. B.; Jellison, G. E.; Hart, F. X. A Stable Thin-Film Lithium Electrolyte: Lithium Phosphorus Oxynitride. *J. Electrochem. Soc.* **1997**, *144* (2), 524–532.

(5) Seino, Y.; Takada, K.; Kim, B. C.; Zhang, L.; Ohta, N.; Wada, H.; Osada, M.; Sasaki, T. Synthesis of Phosphorous Sulfide Solid

Electrolyte and All-Solid-State Lithium Batteries with Graphite Electrode. *Solid State Ionics* **2005**, *176* (31−34), 2389−2393.

(6) Bates, J. Thin-Film Lithium and Lithium-Ion Batteries. *Solid State Ionics* **2000**, *135* (1−4), 33−45.

(7) Zhang, W.; Weber, D. A.; Weigand, H.; Arlt, T.; Manke, I.; Schröder, D.; Koerver, R.; Leichtweiss, T.; Hartmann, P.; Zeier, W. G.; Janek, J. Interfacial Processes and Influence of Composite Cathode Microstructure Controlling the Performance of All-Solid-State Lithium Batteries. *ACS Appl. Mater. Interfaces* **2017**, *9* (21), 17835−17845.

(8) Koerver, R.; Aygün, I.; Leichtweiß, T.; Dietrich, C.; Zhang, W.; Binder, J. O.; Hartmann, P.; Zeier, W. G.; Janek, J. Capacity Fade in Solid-State Batteries: Interphase Formation and Chemomechanical Processes in Nickel-Rich Layered Oxide Cathodes and Lithium Thiophosphate Solid Electrolytes. *Chem. Mater.* **2017**, *29* (13), 5574−5582.

(9) Koerver, R.; Walther, F.; Aygün, I.; Sann, J.; Dietrich, C.; Zeier, W. G.; Janek, J. Redox-Active Cathode Interphases in Solid-State Batteries. *J. Mater. Chem. A* **2017**, *5* (43), 22750−22760.

(10) Kitsche, D.; Tang, Y.; Hemmelmann, H.; Walther, F.; Bianchini, M.; Kondrakov, A.; Janek, J.; Brezesinski, T. Atomic Layer Deposition Derived Zirconia Coatings on Ni-Rich Cathodes in Solid-State Batteries: Correlation Between Surface Constitution and Cycling Performance. *Small Sci.* **2023**, *3* (2), 2200073.

(11) Riegger, L. M.; Schlem, R.; Sann, J.; Zeier, W. G.; Janek, J. Lithium-Metal Anode Instability of the Superionic Halide Solid Electrolytes and the Implications for Solid-State Batteries. *Angew. Chemie Int. Ed.* **2021**, *60* (12), 6718−6723.

(12) Huo, H.; Janek, J. Silicon as Emerging Anode in Solid-State Batteries. *ACS Energy Lett.* **2022**, *7* (11), 4005−4016.

(13) Franco Gonzalez, A.; Yang, N.-H.; Liu, R.-S. Silicon Anode Design for Lithium-Ion Batteries: Progress and Perspectives. *J. Phys. Chem. C* **2017**, *121* (50), 27775−27787.

(14) Sharma, R. A.; Seefurth, R. N. Thermodynamic Properties of the Lithium-Silicon System. *J. Electrochem. Soc.* **1976**, *123* (12), 1763−1768.

(15) Beaulieu, L. Y.; Hatchard, T. D.; Bonakdarpour, A.; Fleischauer, M. D.; Dahn, J. R. Reaction of Li with Alloy Thin Films Studied by In Situ AFM. *J. Electrochem. Soc.* **2003**, *150* (11), A1457.

(16) Wilson, A.; Reimers, J.; Fuller, E.; Dahn, J. Lithium Insertion in Pyrolyzed Siloxane Polymers. *Solid State Ionics* **1994**, *74* (3−4), 249−254.

(17) Bianchini, M.; Roca-Ayats, M.; Hartmann, P.; Brezesinski, T.; Janek, J. There and Back Again—The Journey of LiNiO 2 as a Cathode Active Material. *Angew. Chemie Int. Ed.* **2019**, *58* (31), 10434−10458.

(18) Teo, J. H.; Strauss, F.; Walther, F.; Ma, Y.; Payandeh, S.; Scherer, T.; Bianchini, M.; Janek, J.; Brezesinski, T. The Interplay between (Electro)Chemical and (Chemo)Mechanical Effects in the Cycling Performance of Thiophosphate-Based Solid-State Batteries. *Mater. Futur.* **2022**, *1* (1), No. 015102.

(19) Bianchini, M.; Wang, J.; Clément, R.; Ceder, G. A First-Principles and Experimental Investigation of Nickel Solubility into the P2 Na x CoO 2 Sodium-Ion Cathode. *Adv. Energy Mater.* **2018**, *8* (26), 1801446 DOI: 10.1002/aenm.201801446.

(20) Bianchini, M.; Wang, J.; Clément, R. J.; Ouyang, B.; Xiao, P.; Kitchaev, D.; Shi, T.; Zhang, Y.; Wang, Y.; Kim, H.; Zhang, M.; Bai, J.; Wang, F.; Sun, W.; Ceder, G. The Interplay between Thermodynamics and Kinetics in the Solid-State Synthesis of Layered Oxides. *Nat. Mater.* **2020**, *19* (10), 1088−1095.

(21) Cronk, A.; Chen, Y.-T.; Deysher, G.; Ham, S.-Y.; Yang, H.; Ridley, P.; Sayahpour, B.; Nguyen, L. H. B.; Oh, J. A. S.; Jang, J.; Tan, D. H. S.; Meng, Y. S. Overcoming the Interfacial Challenges of LiFePO 4 in Inorganic All-Solid-State Batteries. *ACS Energy Lett.* **2023**, *8* (1), 827−835.

(22) Mertens, A.; Granwehr, J. Two-Dimensional Impedance Data Analysis by the Distribution of Relaxation Times. *J. Energy Storage* **2017**, *13*, 401−408.

(23) DeWees, R.; Wang, H. Synthesis and Properties of NaSICON-type LATP and LAGP Solid Electrolytes. *ChemSusChem* **2019**, *12* (16), 3713−3725.

(24) Kraft, M. A.; Ohno, S.; Zinkevich, T.; Koerver, R.; Culver, S. P.; Fuchs, T.; Senyshyn, A.; Indris, S.; Morgan, B. J.; Zeier, W. G. Inducing High Ionic Conductivity in the Lithium Superionic Argyrodites Li 6+ x P 1− x Ge x S 5 I for All-Solid-State Batteries. *J. Am. Chem. Soc.* **2018**, *140* (47), 16330−16339.

(25) Krauskopf, T.; Hartmann, H.; Zeier, W. G.; Janek, J. Toward a Fundamental Understanding of the Lithium Metal Anode in Solid-State Batteries—An Electrochemo-Mechanical Study on the Garnet-Type Solid Electrolyte Li 6.25 Al 0.25 La 3 Zr 2 O 12. *ACS Appl. Mater. Interfaces* **2019**, *11* (15), 14463−14477.

(26) Fuchs, T.; Mogwitz, B.; Otto, S.; Passerini, S.; Richter, F. H.; Janek, J. Working Principle of an Ionic Liquid Interlayer During Pressureless Lithium Stripping on Li 6.25 Al 0.25 La 3 Zr 2 O 12 (LLZO) Garnet-Type Solid Electrolyte. *Batter. Supercaps* **2021**, *4* (7), 1145−1155.

(27) Chen, R.; Li, Q.; Yu, X.; Chen, L.; Li, H. Approaching Practically Accessible Solid-State Batteries: Stability Issues Related to Solid Electrolytes and Interfaces. *Chem. Rev.* **2020**, *120* (14), 6820−6877.

(28) Tian, C.; Nordlund, D.; Xin, H. L.; Xu, Y.; Liu, Y.; Sokaras, D.; Lin, F.; Doeff, M. M. Depth-Dependent Redox Behavior of LiNi 0.6 Mn 0.2 Co 0.2 O 2. *J. Electrochem. Soc.* **2018**, *165* (3), A696−A704.

(29) Qiu, J.; Liu, X.; Chen, R.; Li, Q.; Wang, Y.; Chen, P.; Gan, L.; Lee, S.; Nordlund, D.; Liu, Y.; Yu, X.; Bai, X.; Li, H.; Chen, L. Enabling Stable Cycling of 4.2 V High-Voltage All-Solid-State Batteries with PEO-Based Solid Electrolyte. *Adv. Funct. Mater.* **2020**, *30* (22), 1−8.

(30) Xue, Z.; He, D.; Xie, X. Poly(Ethylene Oxide)-Based Electrolytes for Lithium-Ion Batteries. *J. Mater. Chem. A* **2015**, *3* (38), 19218−19253.

(31) Nair, J. R.; Imholt, L.; Brunklaus, G.; Winter, M. Lithium Metal Polymer Electrolyte Batteries: Opportunities and Challenges. *Electrochem. Soc. Interface* **2019**, *28* (2), 55−61.

(32) Hoffman, Z. J.; Shah, D. B.; Balsara, N. P. Temperature and Concentration Dependence of the Ionic Transport Properties of Poly(Ethylene Oxide) Electrolytes. *Solid State Ionics* **2021**, *370* (July), No. 115751.

(33) Deiseroth, H. J.; Kong, S. T.; Eckert, H.; Vannahme, J.; Reiner, C.; Zaiß, T.; Schlosser, M. Li6PS5X: A Class of Crystalline Li-Rich Solids with an Unusually High Li+ Mobility. *Angew. Chemie - Int. Ed.* **2008**, *47* (4), 755−758.

(34) Kamaya, N.; Homma, K.; Yamakawa, Y.; Hirayama, M.; Kanno, R.; Yonemura, M.; Kamiyama, T.; Kato, Y.; Hama, S.; Kawamoto, K.; Mitsui, A. A Lithium Superionic Conductor. *Nat. Mater.* **2011**, *10* (9), 682−686.

(35) Li, Y.; Song, S.; Kim, H.; Nomoto, K.; Kim, H.; Sun, X.; Hori, S.; Suzuki, K.; Matsui, N.; Hirayama, M.; Mizoguchi, T.; Saito, T.; Kamiyama, T.; Kanno, R. A Lithium Superionic Conductor for Millimeter-Thick Battery Electrode. *Science (80-.)* **2023**, *381* (6653), 50−53.

(36) Walther, F.; Koerver, R.; Fuchs, T.; Ohno, S.; Sann, J.; Rohnke, M.; Zeier, W. G.; Janek, J. Visualization of the Interfacial Decomposition of Composite Cathodes in Argyrodite-Based All-Solid-State Batteries Using Time-of-Flight Secondary-Ion Mass Spectrometry. *Chem. Mater.* **2019**, *31* (10), 3745−3755.

(37) Walther, F.; Strauss, F.; Wu, X.; Mogwitz, B.; Hertle, J.; Sann, J.; Rohnke, M.; Brezesinski, T.; Janek, J. The Working Principle of a Li 2 CO 3 /LiNbO 3 Coating on NCM for Thiophosphate-Based All-Solid-State Batteries. *Chem. Mater.* **2021**, *33* (6), 2110−2125.

(38) Ohta, N.; Takada, K.; Sakaguchi, I.; Zhang, L.; Ma, R.; Fukuda, K.; Osada, M.; Sasaki, T. LiNbO3-Coated LiCoO2 as Cathode Material for All Solid-State Lithium Secondary Batteries. *Electrochem. commun.* **2007**, *9* (7), 1486−1490.

(39) Ohta, N.; Takada, K.; Zhang, L.; Ma, R.; Osada, M.; Sasaki, T. Enhancement of the High-Rate Capability of Solid-State Lithium

Batteries by Nanoscale Interfacial Modification. *Adv. Mater.* **2006**, *18* (17), 2226−2229.

(40) Culver, S. P.; Koerver, R.; Zeier, W. G.; Janek, J. On the Functionality of Coatings for Cathode Active Materials in Thiophosphate-Based All-Solid-State Batteries. *Adv. Energy Mater.* **2019**, *9* (24), 1900626.

(41) Zhang, Y. Q.; Tian, Y.; Xiao, Y.; Miara, L. J.; Aihara, Y.; Tsujimura, T.; Shi, T.; Scott, M. C.; Ceder, G. Direct Visualization of the Interfacial Degradation of Cathode Coatings in Solid State Batteries: A Combined Experimental and Computational Study. *Adv. Energy Mater.* **2020**, *10* (27), 1903778 DOI: 10.1002/aenm.201903778.

(42) Ito, Y.; Sakurai, Y.; Yubuchi, S.; Sakuda, A.; Hayashi, A.; Tatsumisago, M. Application of LiCoO 2 Particles Coated with Lithium Ortho-Oxosalt Thin Films to Sulfide-Type All-Solid-State Lithium Batteries. *J. Electrochem. Soc.* **2015**, *162* (8), A1610−A1616.

(43) Jung, S. H.; Oh, K.; Nam, Y. J.; Oh, D. Y.; Brüner, P.; Kang, K.; Jung, Y. S. Li 3 BO 3 − Li 2 CO 3: Rationally Designed Buffering Phase for Sulfide All-Solid-State Li-Ion Batteries. *Chem. Mater.* **2018**, *30* (22), 8190−8200.

(44) Woo, J. H.; Travis, J. J.; George, S. M.; Lee, S.-H. Utilization of Al 2 O 3 Atomic Layer Deposition for Li Ion Pathways in Solid State Li Batteries. *J. Electrochem. Soc.* **2015**, *162* (3), A344−A349.

(45) Moryson, Y.; Walther, F.; Sann, J.; Mogwitz, B.; Ahmed, S.; Burkhardt, S.; Chen, L.; Klar, P. J.; Volz, K.; Fearn, S.; Rohnke, M.; Janek, J. Analyzing Nanometer-Thin Cathode Particle Coatings for Lithium-Ion Batteries−The Example of TiO_2 on NCM622. *ACS Appl. Energy Mater.* **2021**, *4* (7), 7168−7181.

(46) Koerver, R.; Zhang, W.; de Biasi, L.; Schweidler, S.; Kondrakov, A. O.; Kolling, S.; Brezesinski, T.; Hartmann, P.; Zeier, W. G.; Janek, J. Chemo-Mechanical Expansion of Lithium Electrode Materials − on the Route to Mechanically Optimized All-Solid-State Batteries. *Energy Environ. Sci.* **2018**, *11* (8), 2142−2158.

(47) Hertle, J.; Walther, F.; Mogwitz, B.; Schröder, S.; Wu, X.; Richter, F. H.; Janek, J. Miniaturization of Reference Electrodes for Solid-State Lithium-Ion Batteries. *J. Electrochem. Soc.* **2023**, *170* (4), No. 040519.

(48) Lombardo, T.; Walther, F.; Kern, C.; Moryson, Y.; Weintraut, T.; Henss, A.; Rohnke, M. ToF-SIMS in Battery Research: Advantages, Limitations, and Best Practices. *J. Vac. Sci. Technol., A* **2023**, *41* (5), No. 053207, DOI: 10.1116/6.0002850.

(49) Lombardo, T. Https://Github.Com/Teolombardo/User-Friendly-Scripts-for-Experimental-Battery-Researchers.

(50) Bielefeld, A.; Weber, D. A.; Janek, J. Microstructural Modeling of Composite Cathodes for All-Solid-State Batteries. *J. Phys. Chem. C* **2019**, *123* (3), 1626−1634.

(51) Walther, F.; Randau, S.; Schneider, Y.; Sann, J.; Rohnke, M.; Richter, F. H.; Zeier, W. G.; Janek, J. Influence of Carbon Additives on the Decomposition Pathways in Cathodes of Lithium Thiophosphate-Based All-Solid-State Batteries. *Chem. Mater.* **2020**, *32* (14), 6123−6136.

(52) Nakamura, T.; Amezawa, K.; Kulisch, J.; Zeier, W. G.; Janek, J. Guidelines for All-Solid-State Battery Design and Electrode Buffer Layers Based on Chemical Potential Profile Calculation. *ACS Appl. Mater. Interfaces* **2019**, *11* (22), 19968−19976.